The tailsitter autogiro UAV: modeling, design, and CFD simulation

C. Gellida-Coutino, V. Dominguez-De La Cruz, A. Sanchez-Orta, O. Garcia-Salazar, Pedro Castillo Garcia

The tailsitter autogiro UAV: modeling, design, and CFD simulation

C. Gellida-Coutiño [1], V. Dominguez-De la Cruz [2], A. Sanchez-Orta [1], O. Garcia-Salazar [2], and P. Castillo [3]

***Abstract*— This paper focuses on the development of a novel UAV configuration, the convertible tailsitter autogiro, based on simulation and modeling of the most significant aerodynamic and dynamic effects that can affect the autogiro flight during the expected flight conditions. The aerodynamic forces acting on the rotor are simulated using a novel algorithm based on the blade element momentum (BEM) theory (to simulate wind turbines), and on semi-empirical models used for helicopter rotors in autorotation. The tail design is derived from a model of the velocity vector field in the slipstream of the propeller. Finally, aerodynamic control surfaces in the tail are evaluated using a transient k-epsilon Computational Fluid Dynamics (CFD) simulation, which validates the design computation.**

I. INTRODUCTION

The autogiro is a rotary wing aircraft equipped with an engine-driven propeller, which provides forward thrust, and a passive rotor (unpowered) that rotates as a result of the inflow wind due to the aircraft motion, including external wind currents. It is not capable of performing hover flight, however, it is safer than both helicopters and fixed-wing air vehicles due to the absence of the stall velocity, which arises in airplanes at low speeds, and the dead man's curve, which occurs in helicopters. Additionally, the autogiro consumes less energy at moderate speeds [1]. Nevertheless, autogiros have some disadvantages, including the inability to achieve the same speeds as fixed-wing aircraft (as it is the case with helicopters), moreover, autogiros need runways during takeoff and landing, which is shorter than those used by airplanes.

A few air vehicles with passive rotors were proposed to overcome the disadvantages of autogiros; the most well-documented vehicles are the McDonnell XV-1 Convertiplane [2] and the Fairey Rotodyne [3], both incorporate a tip jet engine, which ejects a jet of hot gases and thus enables vertical take off and landing. Despite the fact that both vehicles were capable of flying, they faced problems, especially noise and vibration.

[1] C. Gellida-Coutiño, and A. Sanchez-Orta are with Robotics and Advanced Manufacturing Division, Research Center for Advanced Studies (CINVESTAV), Industria Metalúrgica 1062, Parque Industrial Saltillo Ramos Arizpe, Ramos Arizpe, 25900, México. Email: carlos.gellida@cinvestav.edu.mx, anand.sanchez@cinvestav.mx

[2] V. Dominguez-De la Cruz, and O. Garcia-Salazar are with Aerospace Engineering Research and Innovation Center, Faculty of Mechanical and Electrical Engineering, Autonomous University of Nuevo Leon, Apodaca NL, Mexico. Email: victor.dominguezdlc@uanl.edu.mx, octavio.garciasl@uanl.edu.mx

[3] P. Castillo is with Sorbonne Universités, Université de Technologie de Compiégne, CNRS UMR 7253 Heudiasyc Lab., CS 60319, 60203 Compiégne Cedex, France. Email: pedro.castillo@hds.utc.fr

Several researches have been conducted research on unmanned autogiros vehicles, which have a better performance than multirotors performing foward flight [4], [5], [6]. Additionally, companies such as Carter Aviation Technologies (Carter A.T.) and PAL-V are actively developing V-TOL human scale vehicles based on the autogiro concept. For instance, in Carter A.T., a hybrid airplane-autogiro was offered [7], whilst PAL-V proposed an autogiro equipped with wheels, transmission, and collapsible propeller and rotor that could be used as a car [8].

To address the inability of fixed-wing aircraft to achieve the vertical takeoff and landing, convertible vehicles were proposed. These vehicles can be classified as tilt-rotors, tilt-wing, and tailsitters [9], in which the first two vehicles have a high mechanical complexity and add the weight of additional motors. Convertible tailsitters are mechanically identical to fixed-wing aircraft, but they require a vertical-to-horizontal transition to switch from hover to horizontal flight and vice versa. The main problem with tailsitters is that their wings have a stall velocity, which is the lowest velocity at which they can generate considerable lift force, which means that the vehicle must fly fast enough in order to achieve a smooth transition.

To model the rotor aerodynamics of both helicopters and wind turbines, the blade element momentum (BEM) theory is a feasible option. Nevertheless, this theory fails to describe the autorotation. To overcome this limitation, a semi-empirical engineering correction was proposed in [10], however, the proposed strategy is solved through linearization and simplification of the transcendental equations in BEM theory and using only one control volume. In contrast, in [11], [12] a more sophisticated computational algorithm to solve the transcendental equations was presented. This algorithm allows the control volume to be divided into small control volumes and the blades into sections, however, it cannot directly be applied to describe the autorotation. The formulation of an algorithm to solve the BEM equations with small control volumes and the blade analyzed in sections, as well as the implementation of engineering corrections for autorotation is proposed as part of our contributions.

In this paper, our tailsitter autogiro (TA) is a novel concept that performs the transition from horizontal to vertical flight in a soft manner since the passive rotor can provide an important amount of thrust at low flight speeds. Moreover, the angular velocity of the rotor can be directly measured, allowing the estimation of the rotor thrust, which is useful information for the control algorithm. The main objective of this work is to propose the development of a small TA UAV by using its aerodynamic-dynamic model and simulations

of the flight conditions. To the best of our knowledge, this proposed vehicle has not been published; thus, the proposed approach has not been explored before.

The paper is divided into the following sections: A description of the design algorithm employed to develop the TA is described in section II. The proposed algorithm to estimate the aerodynamic properties of the rotor is presented in section III. The dynamic model using the Newton-Euler formulation is derived in section IV. A novel simple model to describe the flapping motion of blades is presented in section V. The selection of blades and their information generated by applying the proposed novel algorithm to solve the BEM equations are described in section VI. The mass positioning problem is solved and exposed in section VII, while the dimensions and location of the wings in the tail are described in section VIII, which also discusses the fuselage design. A CFD simulation is performed to determine the effect of moment generation on tail and fuselage drag; the results are presented in section IX. Finally, a general conclusion is presented at the end of the paper.

II. Design algorithm

The design objectives include the weight restriction of the vehicle and its endurance, range and autonomy. The problem of design is how to select the design variables such that the design objectives are satisfied while the restrictions imposed by the closed-loops of relations are maintained. A design algorithm based on the spiral principles of design is proposed in [13]. This algorithm yields a solution to the design problem.

The first step of the design algorithm is to select the blades based on the target weight (for instance the blades of a commercial RC autogiro). The second step is to select the motor-propeller so that it provides twice the target weight as thrust force. The third step is to select the battery based on the target time-flight for hover and the propeller-motor power consumption. The fourth step is to define the weight of the fuselage-tail subsystem as the subtraction of the weight of the selected components from the target weight. The fifth step is to propose a tail and fuselage geometry based on aerodynamic models. The sixth step is to propose materials and the structure for the fuselage-tail subsystem to obtain the strength and stiffness that allow flight. This step must be repeated in order to maintain the weight inside a target range. If the full weight exceeds the target weight plus an acceptable gap when the sixth step iterations reach the selected limit, then the rotor must be replaced and the design algorithm begins again, otherwise, a solution of the design is found.

III. Algorithm for simulation of rotor aerodynamics

An important problematic to analyze the TA rotor is that the momentum theory fails exactly in the region when autorotation appears; thus, the classical algorithms used to study helicopter rotors or wind turbines cannot be directly applied. In [10] a model was presented to correct the momentum theory in order to describe the autorotation; however, to the best of our knowledge, this model has not been combined with an algorithm to solve the rotor aerodynamics by segmenting the blades and the rotor disk. Therefore, the correction for autorotation combined with an algorithm is presented in this section.

The first step of this algorithm is to modify the hover velocity definition proposed in [10] in order to describe the flux on partial annular volume control

$$v_h = \sqrt{\frac{\Delta T}{2\rho\,\Delta A}} \tag{1}$$

where $\Delta A = \pi r \Delta r$ is the area of an annular section of the rotor, ρ is the air density and ΔT the axial force generated by such annular section. The climbing ratio in annular control volumes can be then defined as follows

$$l = v_c / v_h \tag{2}$$

where v_c is the local climbing velocity for a given blade section, also known as the free wind velocity for an observer in the section blade frame. The induced velocity at the rotor, in agreement with [10], can be estimated as

$$\frac{v_i}{v_h} = \begin{cases} -\left(\frac{l}{2}\right) + \sqrt{\left(\frac{l}{2}\right)^2 + 1} & \text{if } l > 0 \\ \left(\kappa + \kappa_1 l + \kappa_2 l^2 + \kappa_3 l^3 + \kappa_4 l^4\right) & \text{if } -2 \leq l \leq 0 \\ -\left(\frac{l}{2}\right) - \sqrt{\left(\frac{l}{2}\right)^2 + 1} & \text{if } l < -2 \end{cases} \tag{3}$$

where the case $-2 \leq l \leq 0$ corresponds to the transition region between the wind mill and helicopter regime, κ = 1, κ_1 = -1.125, κ_2 = -1.372, κ_3 = -1.718, κ_4 = -0.655. From [11], the tangential induced velocity, v_t, can be computed as follows:

$$v_t = \sqrt{\frac{\Delta M}{2\rho\,\Delta A (v_c - v_i)}} \tag{4}$$

where ΔM is the aerodynamic moment of the force acting on an annular section of the rotor. Therefore, both the axial and tangential induced velocities at a given annular section of the rotor are estimated. These quantities can be stacked in the induced velocity vector $\boldsymbol{w} = (v_i, v_t)^T$, where v_i and v_t are the magnitude of the axial and tangential velocity, respectively. Thus, the following equations are used [11]:

$$\Delta T = \frac{B(L\cos(\phi) + D\sin(\phi))}{2\pi r F\,\Delta r} \tag{5}$$

$$\Delta M = \frac{B(L\sin(\phi) - D\cos(\phi))}{2\pi r F\,\Delta r} \tag{6}$$

where F is the Prandtl tip lost factor, B is the number of blades, Δr is the width of annulus (which is the same as the

length of blade sections), r is the mean radio of annulus, ϕ is the flux angle given by

$$\phi = \arctan\left(\frac{v_c - v_i}{\omega r + v_t}\right) \tag{7}$$

where ω is the angular velocity of the rotor, while L and D are the lift and drag forces produced by each blade section, respectively, and they can be estimated as follows:

$$L, D = \frac{1}{2}\rho \underbrace{\left((v_c - v_i)^2 + (\omega r + v_t)^2\right)}_{v_{rel}^2} c\, C_i\, \Delta r \tag{8}$$

where c is the length of chord, C_i, for $i \in \{L, D\}$, stands for the lift and drag coefficients, and v_{rel} is the magnitude of the relative wind at each blade section. Finally, the proposed algorithm is given by the pseudocode III.1:

Algorithm III.1: BEM SOLUTION($T, M = f(v_c)$)

```
w ← (0, 0)^T
T ← 0
M ← 0
for r ← r_min to r_max
do { while e < TOL
     do { φ with (7)
          L and D with (8)
          ΔM with (6)
          ΔT with (5)
          v_h with (1)
          l with (2)
          v_i with (3)
          v_t with (4)
          e ← (v_i, v_t)^T − w
          w ← w + k_p e
          e ← ||e||_2
          i ← i + 1
          if i > i_max
            then break
     T ← T + ΔT
     M ← M + ΔM
```

$r_{max} = R$ and ideally r_{min} should be 0, but the relative wing speed is almost axial in the vicinity of the rotor center, posing a convergence problem for the algorithm, thus, $r_{min} = 0.35R$ is proposed. i_{max} is the maximum number of iterations ($i_{max} = 100$ is suggested to achieve convergence). e is an error that feeds a pseudo proportional control, which leads to a soft approximation of the solution. The proportional constant, k_p, must be tuned in such a way that convergence problems caused by the lack of continuity in (3) are overcome.

IV. Dynamic model of the tailsitter autogiro

The TA is considered as a pair of rigid bodies; the main body and the rotor. A reference frame is assigned to each body, denoted by $\boldsymbol{\Sigma_a}$ and $\boldsymbol{\Sigma_r}$, respectively. $\boldsymbol{\Sigma_a}$ is placed exactly at the center of mass of the TA, and $\boldsymbol{\Sigma_r}$ is situated at the middle of the rotor head. Using the Newton-Euler formulation, the equation of motion to describe the attitude dynamics is given by

$$\sum \boldsymbol{m}_{i:a} = \boldsymbol{I_a}\dot{\boldsymbol{\omega}}_{\boldsymbol{a}} + \boldsymbol{\omega_a} \times \boldsymbol{I_a}\boldsymbol{\omega_a} + \boldsymbol{P_R} \tag{9}$$

where $\Sigma \boldsymbol{m_{i:a}}$ is the summation of all the moments of force acting on the TA, $\boldsymbol{I_a}$ is the inertia tensor of the aerial vehicle excluding the rotor. $\boldsymbol{\omega_a}$ is the angular velocity vector expressed in a reference frame whose origin coincides with the center of mass, and $\boldsymbol{P_R}$ is a disturbance due to rotor dynamics, which is computed as follows

$$\boldsymbol{P_R} = \boldsymbol{R_{rot|a}}\left(\boldsymbol{I_{rot}}\dot{\boldsymbol{\omega}}_{\boldsymbol{rot}} + \boldsymbol{\omega_{rot}} \times \boldsymbol{I_{rot}}\boldsymbol{\omega_{rot}}\right) \tag{10}$$

where $\boldsymbol{R_{rot|a}}$ is the rotation matrix that maps the vector coordinates from $\boldsymbol{\Sigma_r}$ to $\boldsymbol{\Sigma_a}$, $\boldsymbol{I_{rot}}$ is the inertia tensor of the rotor, and $\boldsymbol{\omega_{rot}}$ is the angular velocity vector of the rotor expressed as

$$\boldsymbol{\omega_{rot}} = \omega_r \hat{\boldsymbol{z}} + \boldsymbol{R_{rot|a}}\boldsymbol{\omega_a} \tag{11}$$

and

$$\dot{\boldsymbol{\omega}}_{\boldsymbol{rot}} = \boldsymbol{R_{rot|a}}\left(\dot{\boldsymbol{\omega}}_{\boldsymbol{a}} - (\hat{\boldsymbol{z}} \bullet \dot{\boldsymbol{\omega}}_{\boldsymbol{a}})\hat{\boldsymbol{z}}\right) \tag{12}$$

where ω_r is the magnitude of the rotor angular velocity in the frame of the rotor, $\hat{\boldsymbol{z}}$ is a unit vector in the direction of the z axis of $\boldsymbol{\Sigma_a}$ (which is the same for $\boldsymbol{\Sigma_r}$), and $\boldsymbol{R_{rot|a}}$ is a rotation matrix that maps coordinate vectors from $\boldsymbol{\Sigma_r}$ to $\boldsymbol{\Sigma_a}$. The angular acceleration of the rotor is neglected in (12) since no torque is transmitted from the rotor to the main body. Moreover, the forces acting on the rotor are considered to be only parallel to $\hat{\boldsymbol{z}}$, forces acting in other directions are absorbed by the blade flapping motion (which is described in section V). Additionally, the rotor dynamics is considered to be strongly determined by the aerodynamic forces and depends on the free wind. The moments acting on the autogiro are expressed as

$$\sum \boldsymbol{m}_{i:a} = \begin{pmatrix} d_w & d_w & d_w \\ -d_t cos(30^o) & d_t cos(30^o) & 0 \\ d_t sin(30^o) & d_t sin(30^o) & d_t \end{pmatrix} \begin{pmatrix} L_1 \\ L_2 \\ L_3 \end{pmatrix} \tag{13}$$

where d_w is the distance between the vehicle center of mass and the point of intersection of the aerodynamic axis of the wings (PIAA). d_t is the distance between the PIAA and the mean aerodynamic radius of the wings. L_1, L_2, and L_3 are the lift forces of wings. Finally the position dynamics of TA is described as follows

$$\sum \boldsymbol{f_i} = m_a \ddot{\boldsymbol{p}}_{\boldsymbol{a}} \tag{14}$$

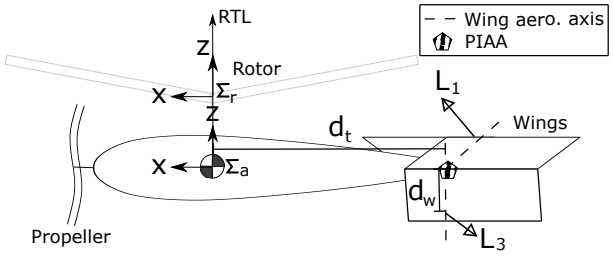

Fig. 1: The schematic diagram of the TA.

where m_a is the mass of the TA (including the rotor) and $\boldsymbol{p_a}$ is the position of the center of mass with respect to the origin of the inertial frame, which is expressed in the coordinates of $\boldsymbol{\Sigma_a}$ and derived in the inertial frame. $\sum \boldsymbol{f_i}$ is the summation of the forces acting on the autogiro that is given by

$$\sum \boldsymbol{f_i} = k_p \omega_p^2 \hat{\boldsymbol{x}} + k_R \omega_r^2 \hat{\boldsymbol{z}} - \frac{\dot{\boldsymbol{p}}_{\boldsymbol{a}}}{|\dot{\boldsymbol{p}}_{\boldsymbol{a}}|} D_a (\dot{\boldsymbol{p}}_{\boldsymbol{a}} \bullet \dot{\boldsymbol{p}}_{\boldsymbol{a}}) + m_a \boldsymbol{g} \tag{15}$$

where k_p is the thrust constant of the propeller, ω_p is the magnitude of the propeller angular velocity, $\hat{\boldsymbol{x}}$ is a unit vector in the direction of the x axis of $\boldsymbol{\Sigma_a}$, D_a is a drag constant of the fuselage and $\boldsymbol{g} = \boldsymbol{R_{0|a}} (0 \quad 0 \quad -9.81)^T$ is the gravitational acceleration vector. $\boldsymbol{R_{0|a}}$ is a rotation matrix that maps vectors from the inertial reference frame to $\boldsymbol{\Sigma_0}$.

V. Blades flapping model

Flapping is the sinusoidal motion of the blades in the same direction as the rotor angular velocity vector, which is caused by an asymmetric moment that arises due to the different relative air velocity acting on each blade. This motion allows autogiros and helicopters to counteract the asymmetric moment by producing an aerodynamic moment with the same frequency and magnitude but in the opposite direction. Despite this benefit, it can cause a collision between the rotor and the autogiro tail, thus, the design process must take into account for the maximum amplitude of oscillations. To accomplish this, in this section, a model, which can be used in autogiros, helicopters, and other rotorcraft of any size, is proposed.

The main objective of this method is to evaluate the case where the blades are flapping but the autogiro is static. Under this condition, a static drag force can be estimated, which generates a static drag moment (M_{Drag}). The flapping motion amplitude can be determined from the static drag moment since it has similar magnitudes to the asymmetric relative wind speed but acts in opposite directions. To derive the proposed model, it is considered that the sum of two wind vector fields has the same aerodynamic forces as those of each vector field, which results from a quasi-linear dependence between lift and drag functions with the angle of attack for small angles, [11]. In addition, the algorithm of the BEM equations presented in section VI is solved assuming small angles in order to obtain the flapping angle that cancels both the asymmetric moment and the static drag moment.

To apply the proposed model, the first step is to define the flapping angle, η, as the angle formed by the tip of the blade relative to itself when the blade is fully tense. Then, the blade drag constant, K_D, is defined, which is used to estimate the moment about the "flap axis" caused by the drag force presented in (17) ($7.7e-3kg \cdot m^2$ for the current blade)

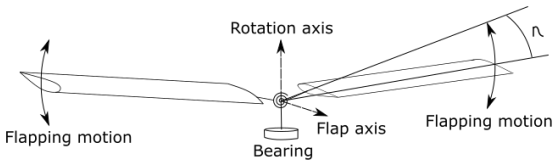

Fig. 2: The schematic diagram of the flapping motion.

$$K_D = B\rho \int_0^R r\, c\, dr \tag{16}$$

which is a general expression, also valid for non rectangular blades. The flapping static moment due to drag force M_{Drag} as a function of flapping angular velocities can be computed as

$$M_{Drag} = -K_D \dot{\eta}^2 sign(\dot{\eta}) \tag{17}$$

Function $M_{Drag}(\dot{\eta})$ in (17) is evaluated within the range $\dot{\eta} \in [-0.3\omega_{max}, 0.3\omega_{max}]$, where ω_{max} is the rotor maximum angular velocity, defined as the value of the angular velocity at which the thrust equals twice the weight of the TA. The obtained curve is linearized using a curve fitting algorithm that corresponds to a first-degree polynomial. The slope of the obtained function is denoted by K_{bl}. Finally, the maximum amplitude of the flapping angle is given by

$$\eta_{max} = -\frac{V_{0,max}\, T_{max}}{\omega_{max}^2 K_{bl}} \tag{18}$$

where $V_{0,max}$ is the maximum free wind velocity of the rotor and T_{max} is the maximum thrust of the rotor.

VI. Estimation of rotor properties via simulation

The selected blades have a constant chord of 4 cm and no torsion, which are classified as rectangular blades. To characterize the airfoil, a photograph of the cross section of a blade is taken and used to generate a point cloud, which is then compared with the airfoils in an airfoil tools database. The airfoil GOE593 is the closest to the point cloud.

The algorithm presented in section III is evaluated for different values of v_c and ω using a function that considers a non-dimensional quantity called tip speed ratio (TSR) as an independent variable,

$$TSR = \frac{\omega R}{v_c} \tag{19}$$

and the thrust and moment coefficients, c_T and c_M, respectively, as dependent variables

$$c_T = \frac{T}{0.5\rho v_c^2 A} \tag{20}$$

$$c_M = \frac{MR}{0.5\rho v_c^3 A} \tag{21}$$

The algorithm is solved for different number of blades $B = [2, 3]$, and using $TOL = 10 - 4$, $k_p = 0.2$, $i_{max} = 100$ and $TSR = [5, 20]$. Fig. 4 and Fig. 3 show the results of the proposed algorithm, where the obtained points are interpolated using a spline interpolation. The algorithm is implemented for two rotors, one with two and the other with three blades. However, for the the three-bladed rotor case, no solution to the design problem has been obtained.

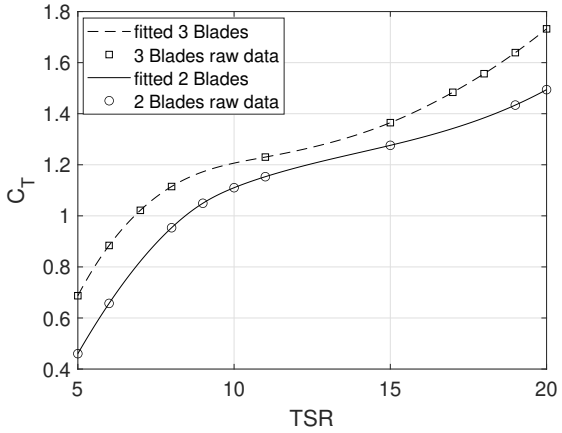

Fig. 3: Thrust coefficient vs tip speed ratio obtained by solving the proposed algorithm.

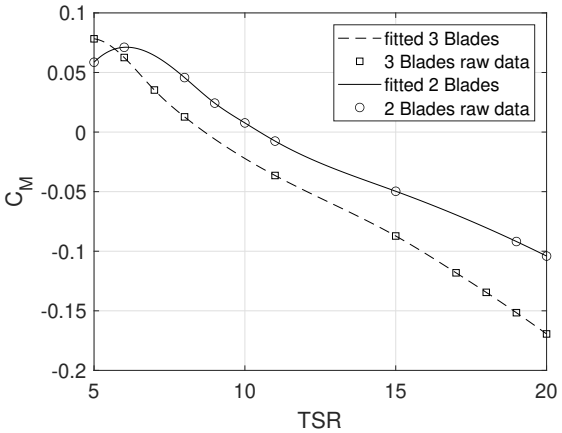

Fig. 4: Moment coefficient vs tip speed ratio obtained by solving the proposed algorithm.

Analyzing Fig. 4 for the three-bladed rotor case, a function that is similar to a straight line with a negative slope can be observed; however, this function must decrease in magnitude until it approaches the point $(0, 0)$, otherwise the law of conservation of energy is violated; this is more evident for the two-bladed rotor case. It can be observed from Fig. 4 that a unique root is obtained at $TSR = 10.5$, for the case of the two-bladed rotor. Therefore, this value represents a stable equilibrium point of the rotor dynamics denoted as TSR_{eq}.

The obtained point by evaluating TSR_{eq} at the thrust coefficient function in Fig. 3 is denoted as the equilibrium thrust coefficient $c_{T,eq}$. The equilibrium thrust coefficients of both rotors are nearly equal; in this case $c_T = 1.14$.

In order to estimate how the rotor behaves when the flow is not axial, a new semi-empirical model is proposed. This model approximates the observed trend in the experimental data reported in [1]:

$$c_T(\alpha) = c_{T,eq} \sin\left(\frac{\pi}{2} \tanh\left(\frac{\alpha_r \pi}{2}\right)\right) \tag{22}$$

Evaluating (22) over some range and using (20), an estimation of how the rotor thrust evolves at different values of v_c and α_r is obtained and presented in Fig. 5.

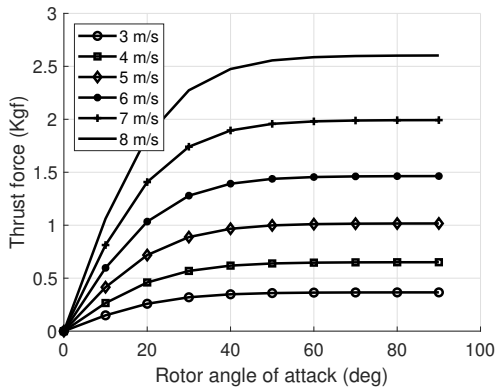

Fig. 5: Estimated thrust force of the rotor at different angles of attack and flight velocity, for both 2 and 3 blades.

Using the curves in Fig. 5, it is possible to deduce that a valid range of weights can be lifted by the blades is from 450gf up to 2000gf; however, in order to avoid exceeding the mechanical resistance of the blade, the weight of the vehicle is considered as 0.55 Kg with a gap of ± 0.1 Kg. Under this consideration, the TA is able to produce sufficient lift with the main rotor at 4 m/s.

Using $c_{T,eq}$ and the data in Fig.3, the angular velocity of the rotor is plotted against the rotor thrust, resulting the data presented in Fig.6, where a quadratic relationship is observed. This demonstrates that the climb velocity has no significant effect on the quadratic tendency. A curve fitting allows determining a quadratic coefficient denoted as b_{rotor}, which is $b_{rotor} = 8.6e-5$ Ns/rad, for the case of the three-bladed rotor, and $b_{rotor} = 5.8e-5$ Ns/rad for the case of the two-bladed rotor.

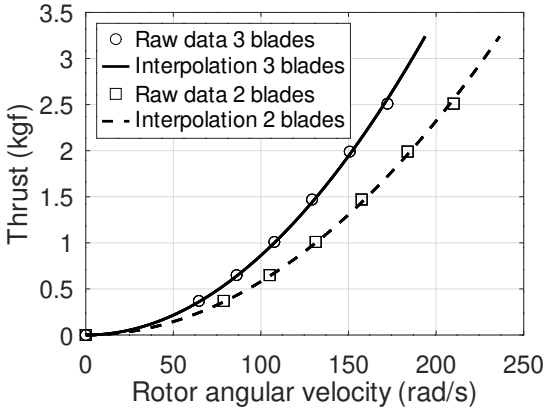

Fig. 6: Thrust vs rotor angular velocity using the data obtained from the solution of the proposed algorithm

Knowing the gyroscopic moment generated by the main rotor is essential for designing the aerodynamic control surfaces; this variable depends on the angular velocity vector of both $\boldsymbol{\omega}_{rot}$ and $\boldsymbol{\omega}_a$ and can be expressed as

$$\boldsymbol{M_{giro}} = I_r \omega_r \boldsymbol{\omega_a} \times \hat{\boldsymbol{z}} \tag{23}$$

where I_r is the moment of inertia about the axis of rotation of the main rotor, which coincides with the TA z axis.

There is no physical reason for limiting rotor gyroscopic moments; however, the control algorithm reduces the inflow angle when the rotor thrust increase in an undesirable manner, maintaining, indirectly, the gyroscopic moment stable. Using (23) and the quadratic curve in Fig. 6, the magnitude of gyroscopic moment is evaluated as a function of the rotor thrust and the vehicle angular velocity, see Fig. 7. From Fig. 7 and with the estimated maximum moment of the tail derived in section IX, a maximum vehicle angular velocity of 0.8 rad/s and a maximum rotor thrust of 700 grams are proposed.

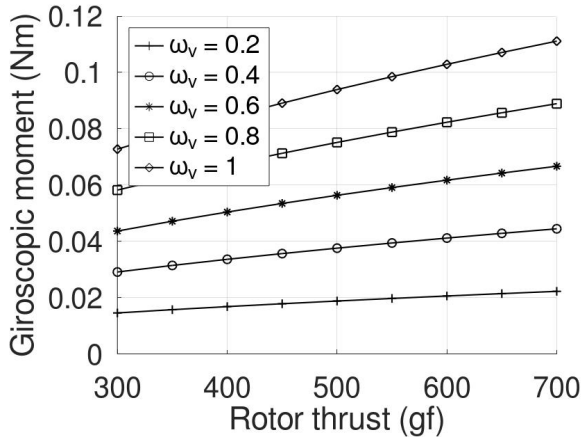

Fig. 7: Magnitude of the gyroscopic moment due to the main rotor thrust and the vehicle angular velocity.

TABLE I: Selected actuators and avionic components

Type	Component	weight (g)
Brushless motor	CRM2413A	170 g
ESC	-	60 g
Battery	LiPo 11.1V (3S)	180g
Embedded	NodeMCU32—Gyro—RF	50g
Servomotor	SG90	9g

VII. Conceptual design and center of mass problematic

According to the design strategy, the motor-propeller, the battery, and other important components are selected; see table I.

The TA can be equipped with either a pusher or a tractor propeller. However, in agreement with recent evidence on small propellers, [14], the slipstream has a greater transverse area as it moves away from the propeller plane. The greater the area of aerodynamic control surface (ACS) submerged in the slipstream, the greater the magnitude of the moment of force provided by the tail. Thus, in order to generate the maximum possible moment, the ACS must be located sufficiently away from the propeller. As a result, the tractor propeller is more convenient for tailsitter applications, thus, this propeller is selected for the proposed UAV. Additionally, designing a tail with the propeller on the front side is easier.

To avoid the moments of force caused by unbalanced payloads, the center of mass of the TA, CM_V, is established at the intersection of the propeller thrust line (PTL) and the rotor thrust line (RTL), which are generally orthogonal in every autogiro when the tilt angle is zero; otherwise, an undesired moment of force is produced, see Fig.8. Using a Cartesian coordinate system with PTL and RTL as axes and the origin at their intersection, an equation for estimating the center of mass over RTL is deduced

$$CM_v = L_r m_{rotor} - L_b m_{batt} - L_e m_{emb} + \sum_{i \in E} L_i m_{emb} \tag{24}$$

where L_b, L_r, and L_e denote the distance between PTL and the battery, rotor, and embedded system centers of mass, respectively. The mass of the battery, rotor, and embedded system are denoted by m_{batt}, m_{rotor} and m_{emb}, respectively. E is a set containing the remainder elements, which are assumed to be distributed symmetrically around RTL, thus, the summation result is approximately zero.

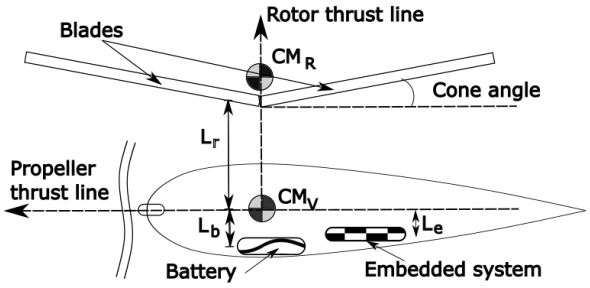

Fig. 8: Main concepts to define the conceptual design.

Even when it is desirable to locate the battery and embedded components as close as possible to the RTL, this is difficult if the condition $CM_v = (0, 0)$ is imposed, as there are some factors that prevent L_r from being small enough. To propose a minimum L_r ($L_{r,min}$), the following assumptions must be established: collisions between the blades and tail are avoided, and the rotor is kept out of the slipstream of the propeller.

The blade coning angle, θ, is the angle formed by the blade longitudinal axis and the plane perpendicular to the RTL. It accomplishes two objectives: to reduce the mechanical loads on the blades and to prevent collisions with the tail. The cone angle is generally equal to the angle formed by the thrust force generated by a blade and the centrifugal force acting on it. Because both the centrifugal and thrust forces depend quadratically on the rotor angular velocity, a constant expression for such an angle is found

$$\theta_{ideal} = \arctan\left(\frac{2\,b_{rotor}}{m_{pala}\,R\,B}\right) \tag{25}$$

where b_{rotor} is the quadratic coefficient defined in section VI. The ideal cone angle should be $5\ deg$ for three and two-bladed rotors. Applying the proposed blade flapping model of section V, the maximum amplitude of the flapping motion is 0.04 rad or 2.29 degrees. Therefore, a cone angle of $5\ deg$ guarantees a balance of the forces over the blades and overcomes the flapping angle.

VIII. Fuselage and control surfaces model design

The slipstream model proposed in [14] is codified. The results of evaluating this model are shown in Fig.9 and Fig.10, where it can be seen that the vector field approaches zero at radial distances greater than 20 cm, indicating that this is the minimum distance to place the rotor-head.

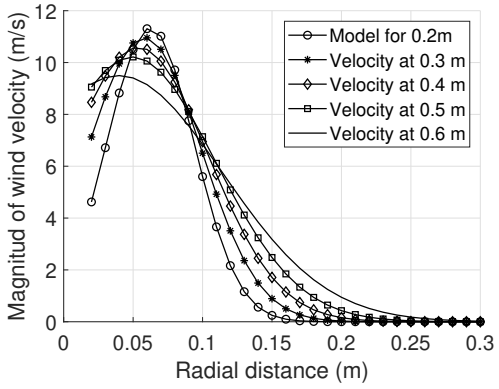

Fig. 9: Magnitude of the velocity vector field of slipstream estimated at 4000 RPM.

The control surfaces in the tail will be referred as wings for practical purposes. The selected airfoil for these wings is the NACA0012. Since the vector field described in Fig. 9 and Fig. 10 is almost zero at a radius greater than 0.2 m, this value is chosen as the wing span. The movable part of

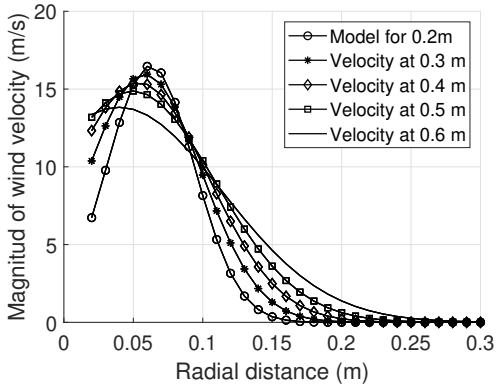

Fig. 10: Magnitude of the velocity vector field of slipstream estimated at 6100 RPM.

wings begins from 75% of the chord to the trailing edge. Three wings are chosen to give stability when the TA is on the ground, each separated by $120\,deg$. The lift and drag coefficients of this airfoil, with the flap turning at $10\,deg$ and $30\,deg$ and at various angles of attack, are obtained through simulations that are conducted using XFOIL, which is a professional software to solve panel method equations to approximate the aerodynamic properties of airfoils [15].

Using the model (13) and the blade element theory, the following equations to estimate the moment provided by the tail wings are obtained

$$M_{roll} = \frac{1}{N_w}\int_0^L 0.5\,W_{act1}\,\rho\,c\,v_{slip}^2\,C_L\,y\,dy \tag{26}$$

$$M_{pitch}, M_{yaw} = \frac{1}{N_w}\int_0^L 0.5\,W_{act2}\,\rho\,c\,v_{slip}^2\,C_L\,x\,dy \tag{27}$$

where W_{acti}, for $i \in [1, 2]$, denotes the number of wings capable of fully providing force to generate moment in that direction, which is three for $i = 1$ and two for $i = 2$, as a result of the selected wing angles. N_w is the number of wings. Evaluating equations (26) and (27) for different distances between the propeller and tail, and chord length, Fig. 11 and Fig. 12 are obtained

The fuselage is shaped based on the NACA0020 airfoil rotating around its chord. The length of the airfoil of the fuselage is 0.6m, which provides sufficient space for the wings to be attached at the calculated distance. The fuselage is constructed using planar pieces cut from balsa wood sheets. To facilitate simple replacement of the battery or internal components, the fuselage is divided into two equal halves, as it is illustrated in Fig. 13. Balsa wood is chosen as the primary material for the fuselage, which is covered with Monokote paper. Extruded polystyrene is used for the aerodynamic control surfaces.

IX. Fuselage and control surfaces CFD simulation

Transient CFD simulation is performed in order to characterize the forces and moments generated by the control

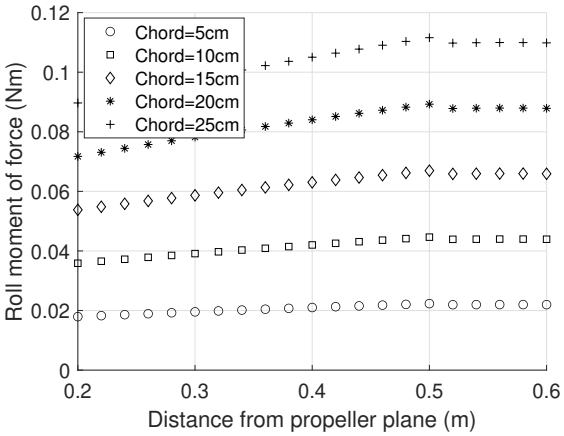

Fig. 11: Estimation of the maximum roll moment generated by the aerodynamic control surfaces on the slipstream.

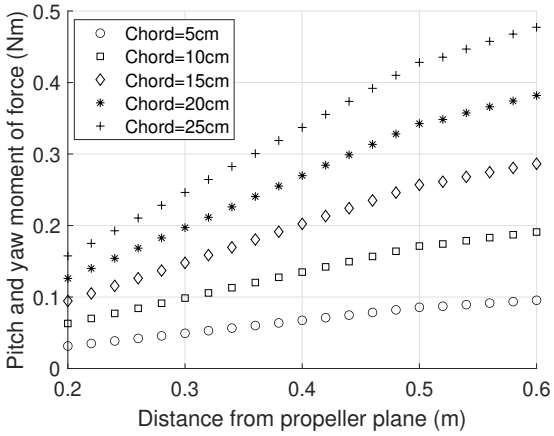

Fig. 12: Estimation of the maximum pitch and yaw moment generated by the aerodynamic control surfaces on the slipstream.

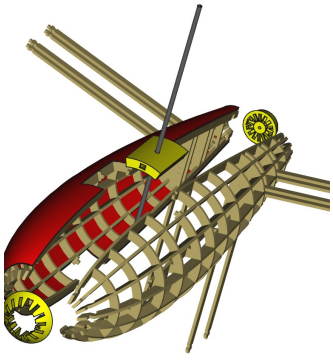

Fig. 13: An exploded view of fuselage main parts.

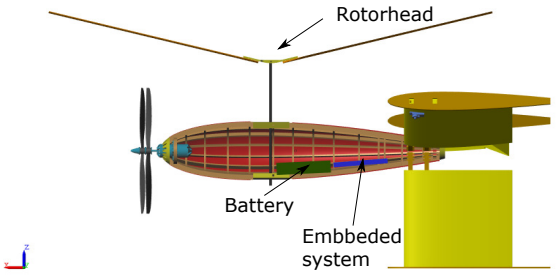

Fig. 14: Position of battery and embedded system inside the fuselage to place the center of mass at thrust lines interception point.

surfaces in relation to the TA center of mass and to validate the proposed model for the tail. This characterization allows the TA hover flight behavior to be predicted. Numerical CFD simulations are carried out using ANSYS Fluent [16]. To conserve computational resources during the analysis, a simplified model is considered, see Fig. 15. The rotor is omitted from this analysis.

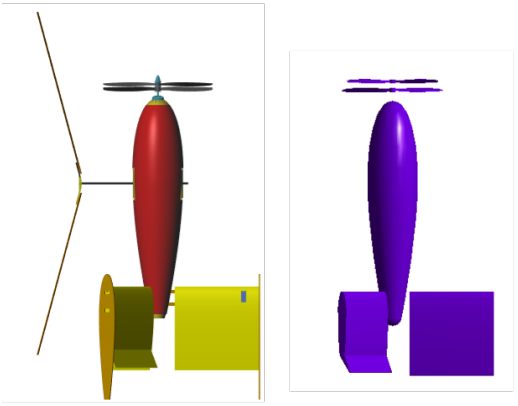

Fig. 15: Tailsitter autogiro simplified model for CFD analysis.

Three distinct control volumes are used in the simulation: one fixed for the fuselage and wings, and two movable for each coaxial propeller. The mesh is generated using the Fluent meshing default setting tool, with body sizes of 1e-4 m for the propellers and 1e-3 m for the remaining bodies.

To solve second-order equations and incompressible flow, a simulation is developed using a pressure-based algorithm and the $k - epsilon$ turbulence model. The system is initialized using hybrid initialization. Up to 20 iterations are performed, and 500 steps are defined with a time value of 0.001 s.

The propellers are turning at different angular speeds in order to avoid the reaction torque observed in previous simulations. It is observed that a relationship of 1.13 exists between the angular velocities, ensuring the least amount of reaction torque.

CFD Results

To visualize the flux around each wing, three planes were chosen, as illustrated in Fig. 16.

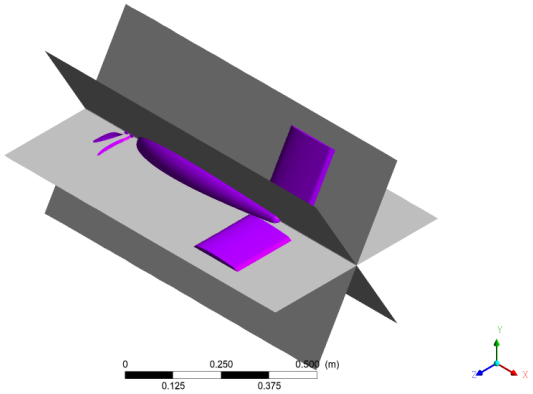

Fig. 16: Independent planes generated over every control surface.

Pressure contours are generated for each generated plane, as illustrated in Fig. 16. Additionally, a velocity contour is generated to quantify the velocity homogeneity around three ailerons in Fig. 18.

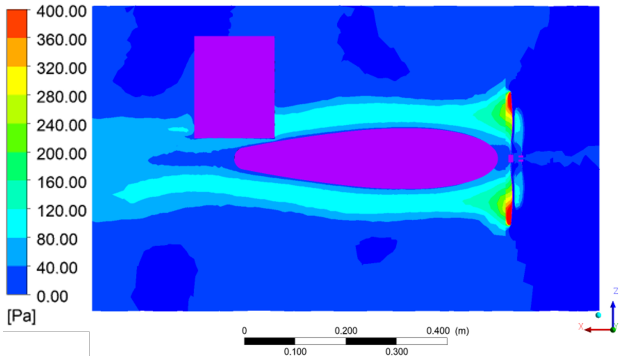

Fig. 17: Pressure contour for 240 deg aileron.

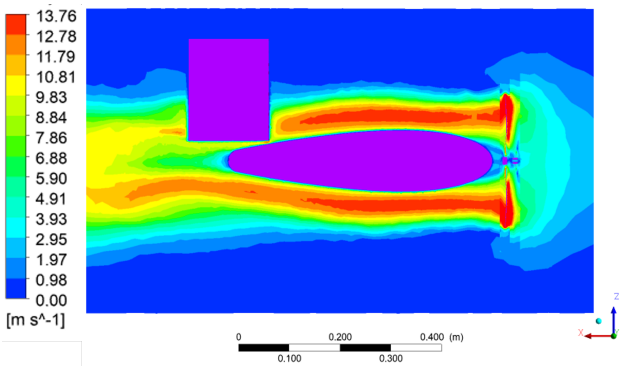

Fig. 18: Velocity contour for 240 deg aileron.

Finally, velocity contours around control surfaces are generated at a distance of 10 cm from the tailsitter center of mass. This enables visualization of the air stream impacting the control surfaces and generating the quantified moments. It is possible to observe that a higher velocity is allocated at the rear of the deflected aileron, implying that this zone receives less pressure, as can be seen in Fig. 19 - 20.

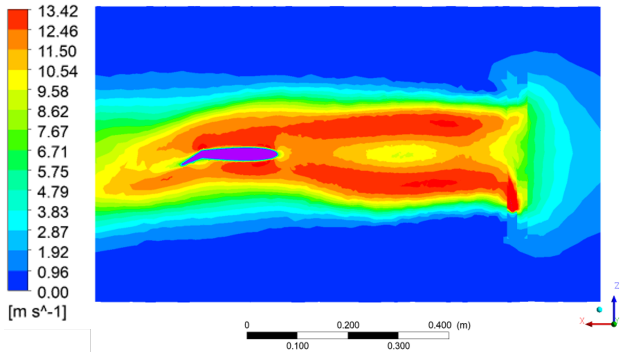

Fig. 19: Velocity contour for 120 deg aileron at 10 cm away from center.

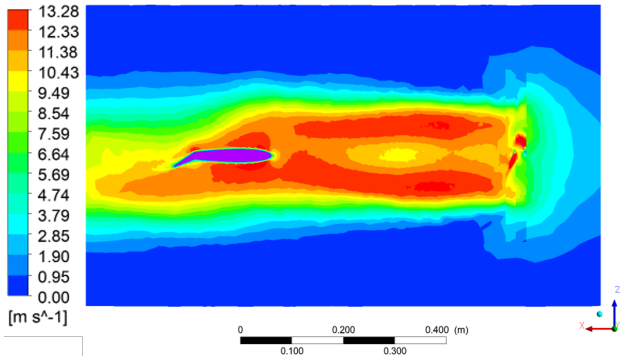

Fig. 20: Velocity contour for 240 deg aileron at 10 cm away from center.

The combined thrust generated by the two propellers is 628 grams-force, simulating hover flight. The moment generated by the three wings is 0.096 Nm per wing on roll moment, which matches acceptably to the 0.089 Nm predicted in section VIII, indicating that the applied technique is valid.

X. Conclusions

The proposed model that describes the aerodynamic forces in hover flight was compared with CFD results, and an acceptable match was found. The proposed algorithm for rotor aerodynamics was implemented to analyze the selected blades, inferring important performance curves of the main rotor to guide the design process. Even if the models are valid for an operation region near to hover, the obtained results confirm that the main rotor can provide sufficient lift at 4 m/s, where the models on the tail are valid. Nevertheless, experimental studies must be performed in order to validate the proposed design methodology. The main goal of this research was the design of a novel tailsitter autogiro configuration based on models and simulation results, in which

the tail overcomes the dynamic and aerodynamic disturbance of the passive rotor.

REFERENCES

[1] J Gordon Leishman. Development of the autogiro: A technical perspective. *Journal of aircraft*, 41(4):765–781, 2004.

[2] Franklin D Harris et al. An overview of autogyros and the mcdonnell xv-1 convertiplane. *NASA/CR, Oct*, 2003.

[3] David Gibbings. The fairey rotodyne—technology before its time? *The Aeronautical Journal*, 108(1089):565–574, 2004.

[4] Enrico Petritoli and Fabio Leccese. Unmanned autogyro for advanced sar tasks: a preliminary assessment. In *2020 IEEE 7th International Workshop on Metrology for AeroSpace (MetroAeroSpace)*, pages 615–619. IEEE, 2020.

[5] Zhihao Cai, Ningjun Liu, Jiang Zhao, and Yingxun Wang. Control and dynamics analysis for miniature autogyro and compound autogyro. *Science China Information Sciences*, 62(1):1–3, 2019.

[6] Enrico Petritoli and Fabio Leccese. Unmanned autogyro for mars exploration: A preliminary study. *Drones*, 5(2):53, 2021.

[7] Jay W Carter Jr and Jeffrey R Lewis. Electric motor powered rotor drive for slowed rotor winged aircraft, May 30 2013. US Patent App. 13/445,594.

[8] Seung Ju Jang. Flying car related technology trends. *European Journal of Engineering and Technology*, 10(1), 2022.

[9] Richard B Bramlette and Ronald M Barrett-Gonzalez. Design and flight testing of a convertible quadcopter for maximum flight speed. In *55th AIAA Aerospace Sciences Meeting*, page 0243, 2017.

[10] Gordon J Leishman. *Principles of helicopter aerodynamics with CD extra*. Cambridge university press, 2006.

[11] Martin Hansen. *Aerodynamics of wind turbines*. Routledge, 2015.

[12] Jens Nørkær Sørensen. The general momentum theory. In *General Momentum Theory for Horizontal Axis Wind Turbines*, pages 43–58. Springer, 2016.

[13] Denis Howe. *Aircraft conceptual design synthesis*, volume 5. John Wiley & Sons Incorporated, 2000.

[14] Waqas Khan and Meyer Nahon. Development and validation of a propeller slipstream model for unmanned aerial vehicles. *Journal of Aircraft*, 52(6):1985–1994, 2015.

[15] Mark Drela. Xfoil: An analysis and design system for low reynolds number airfoils. In *Low Reynolds number aerodynamics*, pages 1–12. Springer, 1989.

[16] PA ANSYS Inc.: Canonsburg. *ANSYS Fluent Theory Guide*. 2013.

[17] Ashish Tewari. *Atmospheric and space flight dynamics*. Springer, 2007.

[18] José Luis Rodríguez Amenedo, Juan Carlos Burgos Diaz, and Santiago Arnalte Gómez. *Sistemas eólicos de producción de energía eléctrica*. Rueda, 2003.

[19] Song Wang, Wan Li Chen, Wen Qiang Dun, Liang Liang Bu, and Fang Chen Dong. Design and experiment of flight path control system of unmanned autogyro. In *MATEC Web of Conferences*, volume 44, page 01065. EDP Sciences, 2016.

[20] SS Houston. Identification of autogyro longitudinal stability and control characteristics. *Journal of Guidance, Control, and Dynamics*, 21(3):391–399, 1998.

[21] Jay W Carter. Extreme mu rotor, January 17 2006. US Patent 6,986,642.